# Atmospheric Pressure Plasma Printing of Nanomaterials for *IoT* Applications

**RAHUL RAMAMURTI[1], RAM P. GANDHIRAMAN [1], ARLENE LOPEZ[1], PRANAY DOSHI[1], DENNIS NORDLUND[1], BEOMSEOK KIM [2,3], AND M. MEYYAPPAN [3] (Fellow, IEEE)**

[1]Space Foundry, Inc., San Jose, CA 95133 USA
[2]Bay Systems, Inc., NASA Ames Research Center, Moffett Field, CA 94035 USA
[3]NASA Ames Research Center, Moffett Field, CA 94035 USA

CORRESPONDENCE AUTHORS: RAM P. GANDHIRAMAN; M. MEYYAPPAN (e-mail: ram@spacefoundry.us; m.meyyappan@nasa.gov)

**ABSTRACT** An atmospheric pressure plasma based printer is described as an alternative to conventional techniques including inkjet printing. The approach is demonstrated to be capable of printing various nanomaterials, and adjusting the plasma parameters, carrier gas flows and the physical parameters of the inks or nanomaterial suspensions can optimize the print quality. Raman analysis was used to characterize the oxide materials and carbon nanotubes printed using this technique, revealing high quality prints. The printed carbon nanotubes were used in a gas sensor chip and shown to provide good ammonia detection capability.

**INDEX TERMS** Plasma jet, printed electronics, nanomaterials, IoT, gas sensor, carbon nanotube.

## I. INTRODUCTION

Printed and flexile electronics has been receiving much attention recently and emerging as an important research area to meet the anticipated demands of the Internet of Things (*IoT*). Ubiquitous deployment of various functional devices in *IoT* applications needs inexpensive manufacturing of devices in different form factors on flexible substrates and even on demand. The anticipated market for flexible and printed electronics is expected to reach $ 250 billion by 2025 due to numerous *IoT* applications. Most functional devices traditionally produced by conventional microfabrication on silicon and other rigid substrates have recently been built on flexible substrates such as polymers, paper and textile [1]–[27]. The printed devices have thus far offered reasonable performance with anticipated further advances in the near future as the technology, materials and processing tools continue to mature. In the mean time, the printed devices exhibit several features desirable in *IoT* applications; for example, they are flexible, foldable, stretchable, biodegradable, disposable, and wearable. To date, almost all fundamental building blocks needed for *IoT* systems have been demonstrated in the form of printable/flexible devices: thin film transistor [1]–[3], memory [4]–[7], battery [8], supercapacitor [9], [10], photovoltaics [11], energy scavengers [12], [13], gas sensors [14]–[16], biosensors and lab-on-paper [17]–[19], heat therapy pad [20], UV sensors [21], pressure and other physical sensors [22], [23], antennas [24], [25], displays [26] and many others [27].

Besides application demonstration, the focus of the research community has been on ink/material development, printing process development, characterization of printed materials and evaluation of material properties needed in flexible applications. The most common printing technique is inkjet printing [28], [29], followed by aerosol printing [30]. Both approaches are capable of printing features as small as sub-10 $\mu$m on various flexible substrates, and commercial printers for research as well as production are available in both cases. One notable characteristic common to these two approaches is that they both need a post thermal annealing or sintering step in order to get a consolidated thin film in most cases. This extra step is time consuming, inconvenient and results in additional thermal budget but more importantly, could preclude the use of delicate substrates depending on the annealing temperature. In contrast, combining cold plasma with aerosol delivery of the ink/nanoparticles can eliminate the need for the secondary annealing step [31]–[33] and also, the use of atmospheric pressure plasma in the form of a dielectric barrier discharge

(DBD) eliminates the need for the expensive vacuum chamber construction and vacuum pumps, thus simplifying the overall system. The characteristics of the plasma jet can be exploited to tailor the properties of the materials passing through it. The material properties including oxidation state, electronic conductivity, dielectric properties and others can be tailored *in situ* through this printing process. The plasma offers several advantages [31]–[33] including i) activation of the material to be printed and the surface to be coated, ii) enhancing the adhesion, iii) precise control over thickness and morphology, and iv) the ability to tailor material properties *in situ*. A robust print head with integrated fluid delivery and power supply that can direct the aerosol to a substrate using electromagnetic field makes it highly suitable not only for terrestrial use but also for space applications.

In the present work, we describe an atmospheric pressure plasma printing system as an alternative to existing techniques and demonstrate printing of nanomaterials such as titanium oxide and tin oxide particles on flexible substrates. In addition, we show the utility of printed carbon nanotubes to function as gas sensors through demonstration of ammonia detection.

## II. EXPERIMENTAL WORK

The plasma here consists of a dielectric barrier discharge of an inert gas such as He or Ar in the print head. A colloidal suspension or ink containing the active material is aerosolized using a nebulizer, which is carried to the plasma using the same carrier gas. Further details are given below.
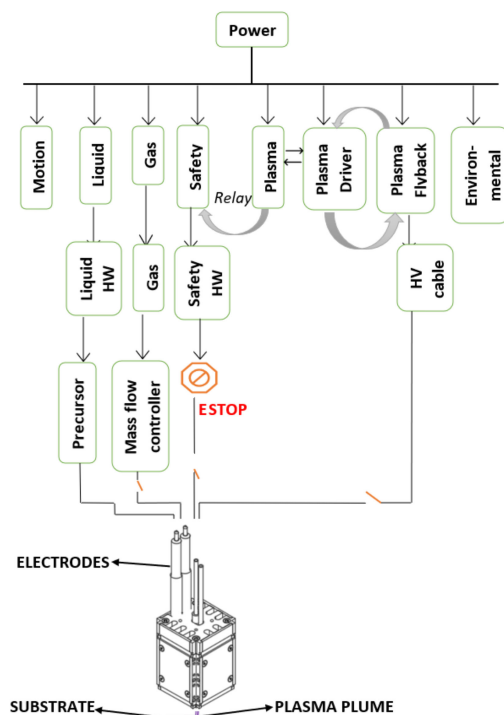
### A. PLASMA JET PRINTER

The plasma jet printing system is fully enclosed in an aluminum metallic frame with electrical and chemical safety engineering and administrative controls (see Fig. 1). The system features a modular design where each major function of the system has a control unit and associated hardware unit. The system consists of motion control, print head gas, liquid, and plasma control, system safety as well as environmental control. The gas, liquid, and plasma control are the major constituents for the atmospheric plasma print head based on the dielectric discharge of gas-mixtures with nebulized particles from a suspended solution.

The motion control is based on a gantry design providing X-, Y-, and Z-motions and industry standard G-code control. The Z-axis has a breadboard that accommodates the print head, gas and fluid. The gas is supplied using mass flow controllers that are controlled by the software. The fluid is supplied using a peristaltic pump and associated valves that are controlled by the software. Options for recirculating the ink and purging of the line are provided in the software. A magnetic stirrer is connected to the fluid delivery system to avoid the settling of nanomaterials in the ink, which also promotes uniform dispersion of the ink. The high voltage power supply operates in the range of 20–60 kHz at voltages below 10 kV. This system has a maximum of 1 A of line power supplied to limit the total power to less than 100 W. Both the voltage and frequency are fully controlled by the
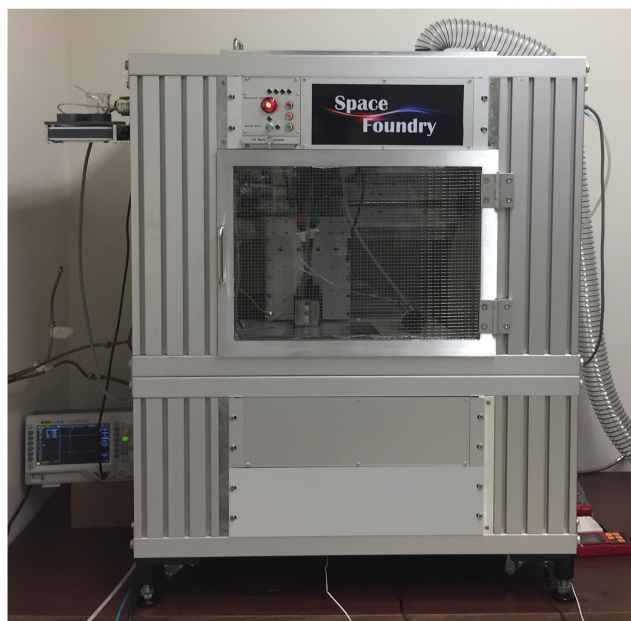


(a)



(b)

FIGURE 1. (a) The plasma printer system with translational and vertical motion of the print head. The printer dimensions are 24″ × 32″ × 42″. (b) Plasma jet printer block diagram.

software via a motorized transformer and potentiometer. The exhaust and a flexible duct connected to the top of the system prevent exposure of aerosolized materials to the user. Safety features have been implemented to provide engineering and administrative controls of the plasma power supply to protect

both the operator and instrumentation from discharges and EMI.

Fig. 1(b) provides a block diagram of the system showing various control units. All the power to the units is controlled by a central circuit breaker that limits the current for the programmable logic control (PLC) system supply. They are referred to system and peripheral 24 V DC power supply, respectively. All the units are supplied from the patch panel that is accessible externally on the back of the system, allowing for testing/integration of new units.
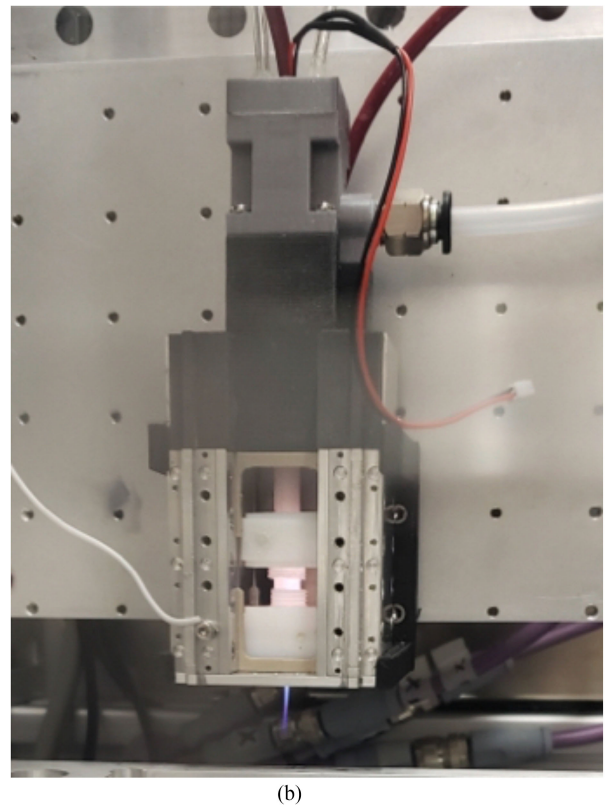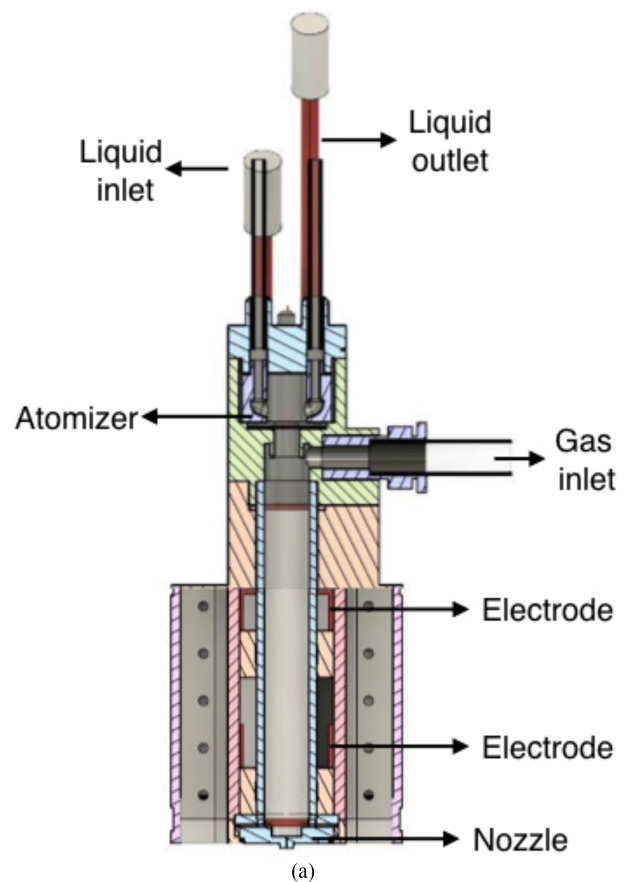
## B. PRINT HEAD

The plasma jet print head consists of a dielectric nozzle with metal electrodes dispersed over it and connected to a high voltage power supply for creating a discharge of an inert gas mixture. One end of the dielectric tube is connected to a manifold through which the carrier gas and material to be printed are introduced in aerosol form; the other end forms a nozzle that is detachable and replaceable with an orifice through which materials from the tube exit in a defined geometry (Fig. 2). The orifice diameter in the detachable nozzle can be varied to control the geometry of printing and resolution. Aerosolized ink is introduced to the dielectric nozzle by the carrier gas and passes through the plasma region before directed to the substrate. The aerosolized material, upon entering the plasma region, is subjected to a combination of electrical and magnetic fields, electro-hydrodynamic forces and bombardment by plasma species. The material to be printed is accelerated out of the nozzle with a momentum created by the externally applied electric field and plasma to enable focused expulsion of the material and print in a geometrical fashion resulting in high density of materials directed through the nozzle.

## C. INTEGRATED FLUID DELIVERY

In order to increase the efficiency and reliability of printing, the density, flow rate, droplet size, atomization rate and the size distribution of the aerosolized particles need to be efficiently controlled. An efficient way to introduce aerosolized particles to the plasma jet print head is to place the atomizer closer to the print head using a modular fluid delivery assembly that can be attached and detached from the print head. High controllability of droplet size and volume is important to obtain consistent results if the plasma process parameters are optimized. A piezo electric nebulizer controls the droplet size here. The plasma print head allows non-clogging features and also *in situ* plasma based cleaning to remove any materials deposited on the inner walls of the dielectric tube where the plasma is generated. The core portion of the print head is made of corrosion-resistant materials allowing for a wide range of precursors to be introduced into the plasma.

The fluid delivery assembly attached to the print head comprises of an ink reservoir, piezo electric atomizer, fluid inlet and gas inlet as shown in Fig. 2(a). The atomizer contains a piezoelectric vibrator that generates aerosol when the liquid comes in direct contact with it, and it is placed inside the ink



(a)



(b)

**FIGURE 2.** (a) Schematic of the print head. b. Image of the print head (50 mm × 180 mm).
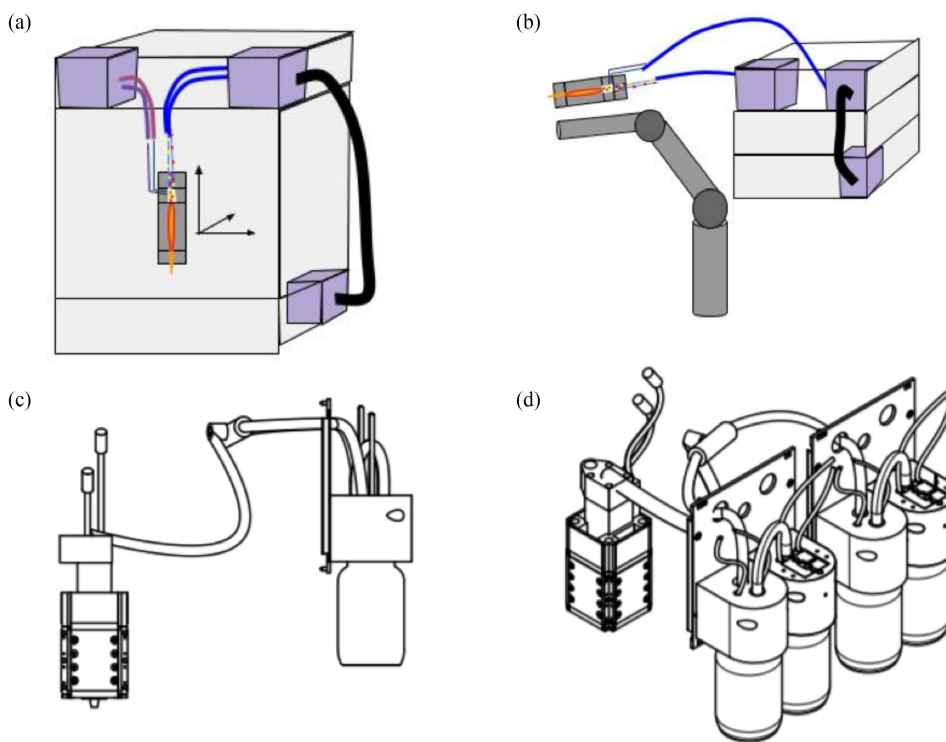
**FIGURE 3.** Schematic showing different configurations of the printer and print head. (a) Stand alone printer with single print head; (b) robot mountable OEM print head; (c) single ink fluid management print head; and (d) multi-ink fluid management print head.
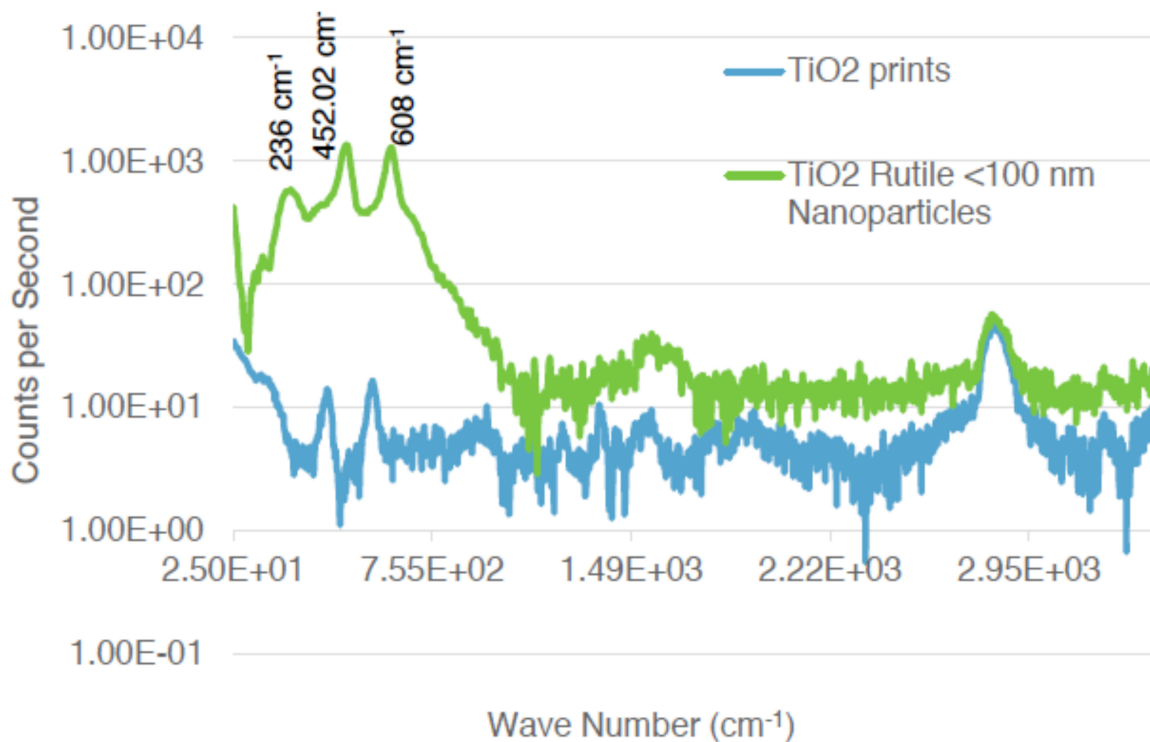


**FIGURE 4.** Raman spectra of $TiO_2$, comparing the nanoparticle powder precursor and the printed layer showing match of peaks at 236, 452 and 608 $cm^{-1}$.
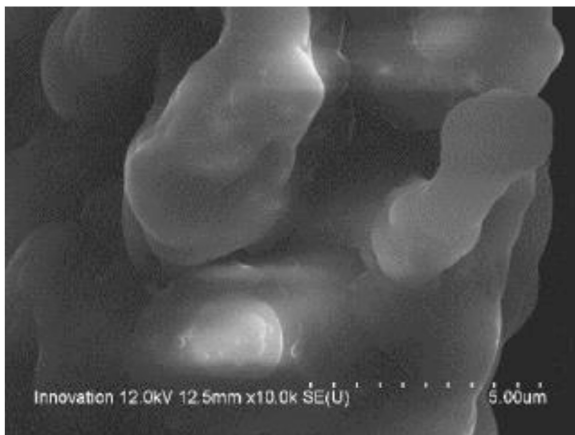
(a)
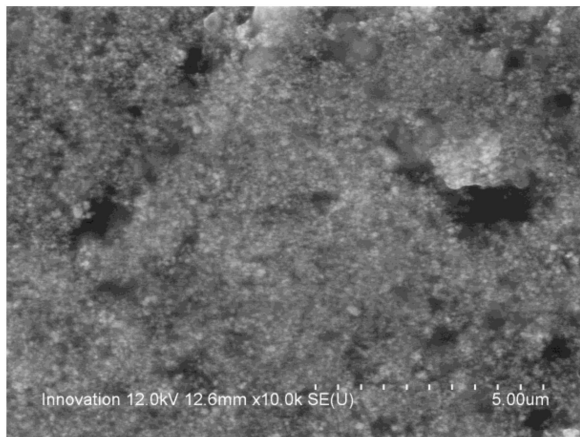


(b)



(c)

**FIGURE 5.** SEM images of printed layers: (a) $TiO_2$ on silicon; (b) $SnO_2$ on PCB chip. (c) Patterned print of $SnO_2$ on a glass slide (75 mm × 25 mm).

reservoir. The liquid inlet and outlet help to re-circulate the ink while the atomizer at the bottom of the reservoir continuously aerosolizes the ink. The aerosol is carried by the gas towards the plasma jet printer, where the materials in the aerosol are accelerated by the plasma towards the substrate.

### D. PRINTING AND CHARACTERIZATION

The plasma printer was used to print some representative materials that might find applications in the emerging *IoT* field. Titanium oxide has been widely used to fabricate memristors both on hard and flexible substrates [34]. Low temperature

printing of high quality thin films is critical to accelerate the memristor technology for the emerging memory and neuro-morphic computing applications. Tin oxide has long been used in gas sensing applications due to its response to various gases and vapors [35], and sensing devices have been constructed in the form of chemiresistors and chemical field effect transistors [36], [37]. Metal oxides in general are widely explored for photo catalysis, energy conversion and in sensors. Titanium dioxide has been explored in microelectronic applications as an alternate for silicon dioxide dielectric. Low leak-age current and high dielectric constant of titanium dioxide are attractive features. Single wall carbon nanotubes (SWCNTs) have found diverse applications including gas sensors and most recently, in flexible gas sensors printed on polymer and paper substrates [38]–[40]. Plasma printing can be effectively used to print diverse materials, and printing results for the above three materials are described in the next section.

High magnification images of all the printed samples were obtained using a Hitachi S-4800 Field Emission Scanning Electron Microscope with light element analysis using Oxford INCA Energy Dispersive Spectroscopy (EDS). The instrument has a resolution of 1-2 nm and a dual secondary emission detector comprising of a lower detector for surface topography imaging and an in-lens upper detector for high-resolution imaging. A back-scattered electron detector allows for imaging insulating samples. The magnification ranges from 20–800 kx. Raman analysis was carried out using a ThermoDXR Micro Raman Instrument equipped with a dispersive microscope with a removable Class 1 laser enclosure.

### E. STAND ALONE, OEM MOUNTABLE AND MULTI-MATERIAL PRINT HEAD

The printer used for this study is a stand-alone printer as shown in Fig. 1. Different print head configurations that can be used as a standalone printer, Original Equipment Manufacturer (OEM) mountable print head and multi-material printing are shown in Fig. 3. In Fig. 3(a), the print head is connected to a small xyz stage inside the printer, allowing the print head to print on both planar and non-planar substrates. For additive manufacturing applications, the print head needs to be mounted on a robotic arm or with other additive manufacturing equipment as shown in Fig. 3(b). The print head and integrated fluid delivery design allows integrating the print head to a robotic arm enabling additive direct write printing on 3D objects. The print head in this case includes all the hardware interfaces for basic control functionality of the printing process including gas, liquid and power. The control units for gas, liquid, gantry etc. are mounted on a standard rack unit.

The fluid delivery management design is scalable for more than one precursor. Fig. 3(c) shows the configuration for single material printing. The design is capable of various combinations that include varying of gas flow rate and aerosol flow rate for multi-material deposition. Multiple fluid delivery management units can be added in parallel for multi-material deposition. Fig. 3(d) shows the feeding of two inks into the print head.
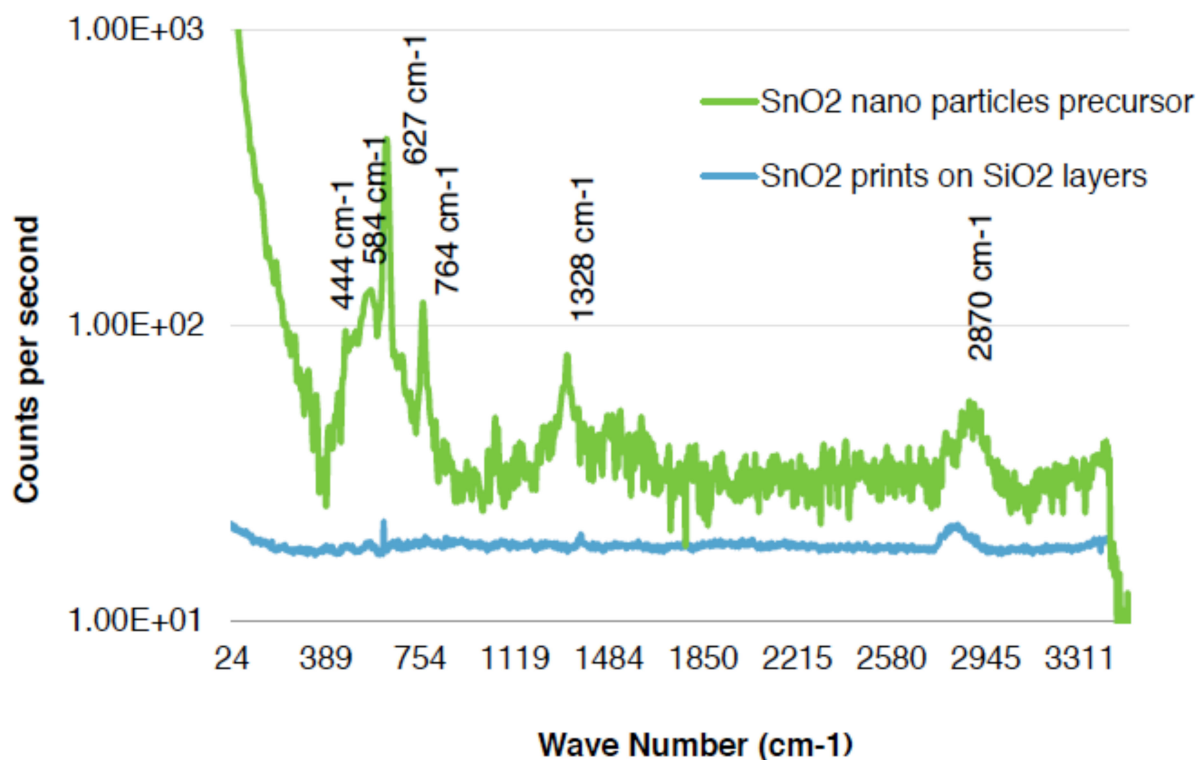
**FIGURE 6.** Raman spectra of SnO$_2$ comparing nanoparticle feed powder and printed layer.
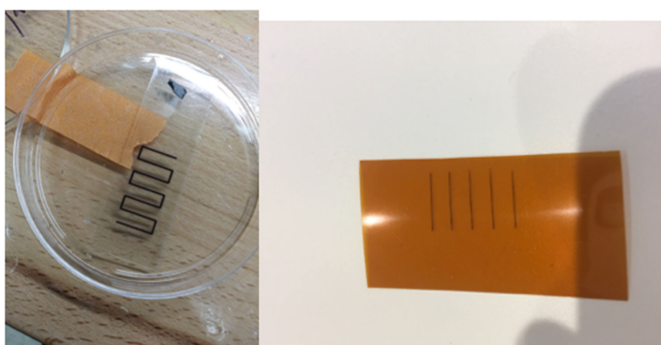


**FIGURE 7.** Copper oxide printed on a glass slide (75 mm × 25 mm) with printed line dimensions of 15 mm separated by 5 mm (left) and 10 mm lines printed on polyimide (right).

## III. RESULTS AND DISCUSSION

### A. TiO$_2$ PRINTING

A suspension of <100 nm TiO$_2$ particles in ethanol was made for the printing process by mixing 0.0812 g of TiO$_2$ powder in 20 ml ethanol. The TiO$_2$ printing was influenced by several factors: (a) number of passes of the print head, for example 1-4 passes; (b) nozzle tip diameter, ranging from 0.6 to 3.5 mm; (c) the z-distance between the print head and the substrate, varied between −3 and −7 mm; (d) a resonant plasma frequency ranging from 26 kHz to 28 kHz; (e) atomization, which can range from 26 to 44% depending on the Ar and He gas flow; (f) Ar/He flow of 600–1500 sccm; g) a scan rate of 0.1–0.5 mm/sec; and h) a fluid pumping rate ranging up to 2.0 mL/min.

Raman spectroscopy is a powerful tool to identify the crystal phases in TiO$_2$. Fig. 4 shows the Raman spectra of the rutile phase of the nanoparticles with a slight broadening, which is due to the background and indicative of the nanoparticle size of the powder rather than a lack of crystallinity. We can see that there is a match in the peaks between the printed TiO$_2$ and the nanoparticle powder precursor with the matching peaks at 236, 442 and 608 cm$^{-1}$. The peak at 2860 cm$^{-1}$ is due to water molecules, indicating that there is water adsorbed on the surface of the print. The intensity of this peak decreases with increasing depth of acquisition. It is valuable to explore Raman scattering using a low wavelength laser (possibly in the UV) in order to obtain a significant Raman signal from the prints that are not very dense and with low thickness. In the visible part of the spectrum (633 nm He Ne laser), light will penetrate 3 $\mu$m whereas the penetration depth at 785 nm is about 12 $\mu$m, dropping to 0.7 $\mu$m at 532 nm [41]. For lasers emitting in the UV range, the penetration depth is in the range of 5–10 nm. So, it is advantageous to use a 455 nm laser when obtaining Raman scattering from TiO$_2$ and SnO$_2$ prints [41]. Raman spectra were collected using the 455 nm laser on the TiO$_2$ printed over SiO$_2$ layers as shown in Fig. 4. This spectrum is compared with the spectra of the TiO$_2$ rutile phase nanoparticles acquired using a 532 nm laser. There is good match of the peaks from the prints compared with those from the powder sample. The peak positions of the printed samples are at 238, 452 and 611 cm$^{-1}$ and the corresponding
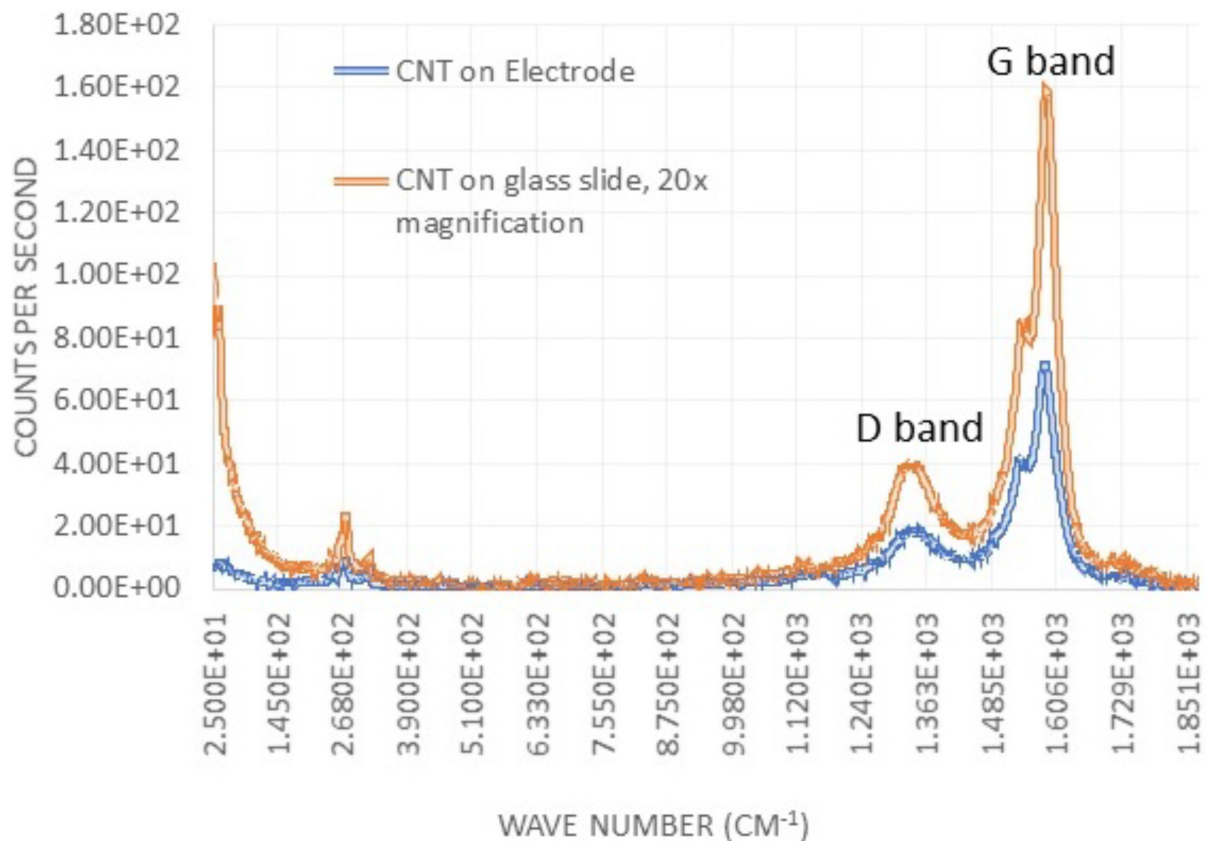
**FIGURE 8.** Raman spectra of SWCNTs printed on glass slide and a PCB gas sensor chip electrode.

intensities are lower than those for the powders due to the lower thickness of the printed sample. The band position shift is due to thickness, stress/strain and deformation [41]. The image of a printed $TiO_2$ sample is shown in Fig. 5(a) revealing that the $TiO_2$ print is in the form of nodules. The nodular growth of the print on the substrate would reduce the RMS thickness, which is good for the overall quality of the prints. As interest is surging in printing memristors on flexible substrates [5], the plasma printer can meet the needs of printing $TiO_2$ and other oxides suitable for memristor applications.

### B. SnO₂ AND COPPER OXIDE PRINTING

The precursor for printing $SnO_2$ was <100 nm nanoparticles in ethanol suspension at two concentrations of 0.00431 and 0.00816 g/ml. A discharge with a resonant plasma frequency in the range of 26 to 28 kHz was ignited and the nanoparticles were carried by the inert gas through a nozzle of diameter 0.6 mm to 3.5 mm. The distance between the print head and the substrate ranged from −3 mm to −7 mm. Fig. 5(b) shows a SEM image of the print of $SnO_2$ on a printed circuit board (PCB) chip and Fig. 5(c) shows a patterned print of $SnO_2$ on a standard glass slide substrate, characteristic of small diameter nozzles. The Raman spectra of the tin oxide nanoparticles versus the plasma printed samples are shown in Fig. 6. The prominent peaks for $SnO_2$ nanocrystalline powder and prints are 444, 584, 764, 1052 and 1328 $cm^{-1}$. The peak at 2870

$cm^{-1}$ due to water molecules is indicative of water being adsorbed on the surface. The peak heights are small for the printed samples, and the match of the peaks with the powder is not obvious. In addition to tin oxide, we also printed copper oxide in a similar way with <100 nm nanoparticles in ethanol suspension and the corresponding results for printing on a glass slide and polyimide are shown in Fig. 7. Copper oxide lines can be easily reduced to copper *in situ* if helium is diluted with about 5% hydrogen as shown in ref. 33 and this is an effective approach to obtain copper lines directly for antennas and other applications from an inexpensive oxide precursor. This versatility is unique to the plasma jet printer unlike in other techniques.

The printing resolution is controlled by the nozzle diameter and currently the maximum printing resolution that can be achieved with the existing print head is 700 microns. Further development to demonstrate print resolution in the range of 10s of microns is in progress. The plasma jet technology does not pose a limitation on high resolution as the fluid flow in the nozzle is controlled by electromagnetic field and plasma. The aerosol droplets in the range of 100s of nm to few microns can flow through the nozzle, directed by the plasma jet without condensing inside the nozzle. The minimum film thickness that can be deposited varies with the type of materials. For example, printing thickness in the range of 10s of nm is possible for a dielectric such as silicon dioxide. The

minimum thickness can only be 100s of nm for $TiO_2$ and $SnO_2$ printed using 80–100 nm sized nanoparticles. With smaller sized nanoparticles (10–20 nm), a minimum thickness in the range of 100 nm can be obtained. The plasma jet printing technology allows multiple process parameters to be optimized to tailor the film thickness, film porosity, uniformity, conductivity, dielectric constant, surface chemistry etc. The process parameters that can be controlled are applied power, gas mixtures (inert, reducing, oxidizing gases), precursors, flow rate of ink and gas, working distance, plasma density, and electron and ion density.

## C. SWCNT PRINTING

The SWCNT suspension was directly injected into the fluid delivery unit to avoid the clogging of the lines and valves commonly associated with CNT-based solutions. A flow rate of 611 sccm of argon was used with an atomization of 49.5% maintaining a good degree of mist formation. Raman analysis of the printed SWCNTs was done to check the presence of characteristic peaks for carbon, which usually include peaks at 1340–1350 $cm^{-1}$ (D peak) and 1550–1600 $cm^{-1}$ (G peak). The narrower the peak with high intenstiy, the higher is the crystallinity. Fig. 8 shows the Raman plots of SWCNTs printed on a glass slide and also on a PCB chip electrode meant for gas sensing applications. The G and D peaks for the print on a glass slide have a smaller full width at half maximum (FWHM) and higher peak intensity than the corresponding peaks for the prints on the electrode, indicating higher crystallinity. The differences may be due to the difference in film thickness. Also, the Raman spectra confirm that the material deposited indeed is single-wall carbon nanotube.

SEM images of the SWCNT prints are shown in Fig. 9 where the nanotubes were deposited on a PCB chip consisting of 16 sensors suitable for gas sensing. The resistance across all 16 channels of the PCB chip is in the range of 255 ohms to 2 Mohms, favorable for gas sensing applications [40]. In principle, multiple materials up to sixteen different candidates (CNTs, graphene, oxides etc.) can be printed on sixteen different channels for the construction of electronic nose [15] but only two different types CNTs (pristine and carboxylic functionalized) were deposited here on a few channels using the plasma printer to demonstrate the functioning of a gas sensor. The plasma printed SWCNT sensor was exposed to varying concentrations of ammonia at room temperature as shown in Fig. 10. The sensor response is given by SR = (R-$R_0$)/$R_0$ where R is the instantaneous resistance and $R_0$ is the baseline resistance or initial resistance before gas exposure. The sensor responses are 1.8%, 4.5% and 10.1% for 10, 30 and 75 ppm of $NH_3$ respectively in Fig. 10 for the pristine SWCNTs. The detection limit is normally estimated [15] by $3 * RMS_{noise}$ /slope, where $RMS_{noise}$ is the root mean square of the noise and slope refers to that of the calibration curve (Fig. 10 inset); the estimated detection limit is 150 ppb for the printed sensor. In another channel of the sensor chip using carboxylic acid functionalized SWCNTs, the corresponding responses were higher at 2.5, 15 and 24%. The sensor response
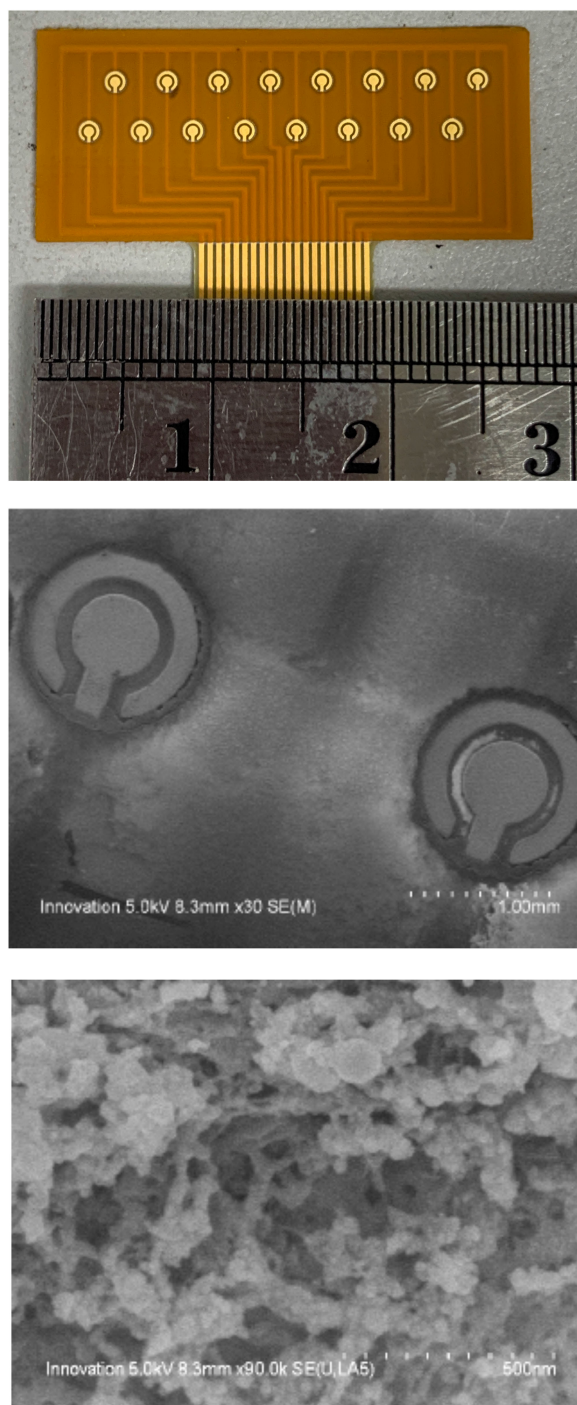


**FIGURE 9.** Photograph of a PCB 16-sensor chip (top), SEM images SWCNTs printed on the sensors (middle) and enlarged view of the printed carbon nanotubes (bottom).

and detection limit obtained here are comparable to previous ammonia sensors on flexible and other substrates [39], [40], [42], [43] confirming the suitability of the plasma printed samples for gas sensing applications. Additional variations in nanotubes can include doping, different functionalizations [42], metal loading etc. with preparation of the corresponding
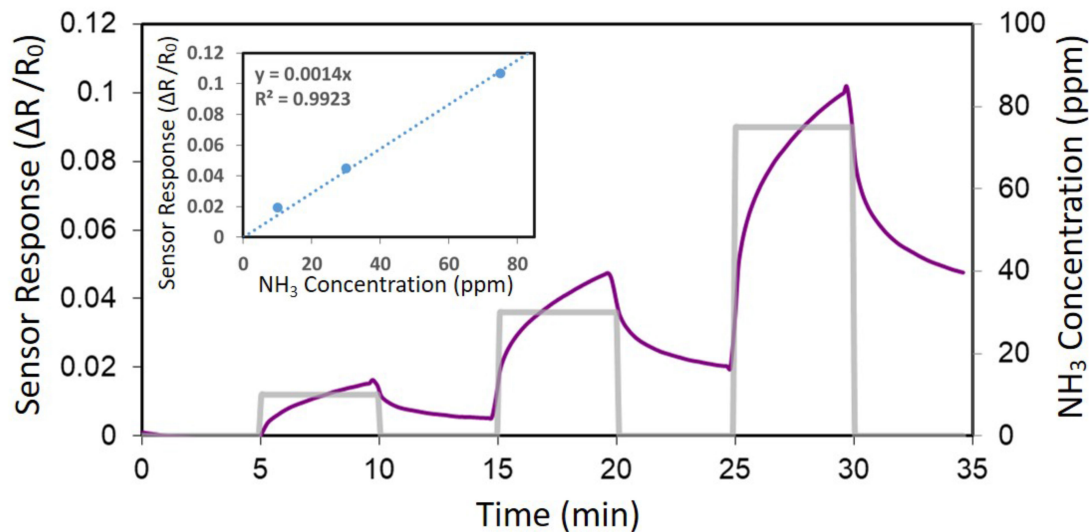
**FIGURE 10.** Representative gas sensing results for a printed SWCNT sensor for exposure to 10, 30 and 75 ppm of ammonia. Gray line shows the ammonia concentration administered over time and the purple line represents the corresponding sensor response. The inset shows the calibration curve of sensor response vs. ammonia concentration.

inks; such wide material variations can be handled by this approach allowing printing different inks on different channels for electronic nose construction [15]. The use of PCB-based chips in smart phones for environmental monitoring has been previously demonstrated [43] and the plasma printing can provide a potential technology for the automated printing of multimaterials in a sensor array.

## IV. CONCLUSION

We have demonstrated direct atmospheric pressure plasma jet printing of various materials using a versatile tool and approach capable of printing a range of inorganic and organic materials. The generated plasma is in the form a fine plume, which can be tuned by varying the diameter of the nozzle. Titanium dioxide, tin dioxide and single wall carbon nanotubes were successfully printed on various substrates including glass, silicon and silicon dioxide layers and PCB chips. The quality of the plasma-printed materials is dependent on several deposition factors including carrier gas flow rate, resonant plasma frequency, nozzle diameter and others, and optimization of these parameters can lead to desirable deposition conditions as demonstrated here. Finally, direct deposition of SWCNTs on a gas sensor chip was accomplished using the plasma printer and the sensor chip showed effective response to various concentrations of ammonia.

## REFERENCES

[1] S. H. Ko, H. Pan, C. P. Grigoropoulos, C. K. Luscombe, J. M. J. Fréchet, and D. Poulikakos, "All-inkjet-printed flexible electronics fabrication on a polymer substrate by low-temperature high-resolution selective laser sintering of metal nanoparticles," *Nanotechnology*, vol. 18, 2007, Art. no. 345202.

[2] S. Kyung, J. Kwon, Y. Kim, and S. Jung, "Low-temperature, solution-processed, 3-D complementary organic FETs on flexible substrate," *IEEE Trans. Electron Devices*, vol. 64, no. 5, pp. 1955–1959, May 2017.

[3] S. Jang, S. Kim, M. L. Geier, M. C. Hersam, and A. Dodabalapur, "Inkjet printed carbon nanotubes in short channel field effect transistors: Influence of nanotube distortion and gate insulator interface modification," *Flex. Print. Electron.*, vol. 1, 2016, Art. no. 035001.

[4] B. Huber, P. B. Popp, M. Kaiser, A. Ruediger, and C. Schindler, "Fully inkjet printed flexible resistive memory," *Appl. Phys. Lett.*, vol. 110, 2017, Art. no. 143503.

[5] K. J. Yoon et al., "Electrically-generated memristor based on inkjet printed silver nanoparticles," *Nanoscale Adv.*, vol. 1, pp. 2990–2998, 2019.

[6] D. H. Lien, Z. K. Kao, T. H. Huang, Y. C. Liao, S. C. Lee, and J. H. He, "All-Printed paper memory, *ACS Nano*, vol. 8, pp. 7613–7619, 2014.

[7] K. Rajan, E. Garafalo, and A. Chiolerio, "Wearable intrinsically soft, stretchable, flexible devices for memories and computing," *Sensors*, vol. 18, 2018, Art. no. 367.

[8] A. M. Gaikwad, A. C. Arias, and D. Steingart, "Recent progress on printed flexible batteries: Mechanical challenges, printing technologies, and future prospects," *Energy Technol.*, vol. 3, pp. 305–328, 2015.

[9] H. Zhang, Y. Qiao, and Z. Lu, "Fully printed ultraflexible supercapacitor supported by a single-textile substrate," *ACS Appl. Mater. Interfaces*, vol. 8, pp. 32317–32323, 2016.

[10] M. L. Seol et al., "All-printed in-plane supercapacitors bysequential additive manufacturing process," *ACS Appl. Energy Mater.*, vol. 3, pp. 4965–4973, 2020.

[11] F. C. Krebs, "Fabrication and processing of polymer solar cells: A review of printing and coating techniques," *Sol. Energy Mater. Sol. Cells*, vol. 93, pp. 394–412, 2009.

[12] Y. Qi, N. T. Jafferis, K. Lyons, C. M. Lee, H. Ahmad, and M. C. McAlpine, "Piezoelectric ribbons printed onto rubber for flexible energy conversion," *Nano Lett.*, vol. 10, pp. 524–525, 2010.

[13] M. L. Seol, J. W. Han, D. I. Moon, K. J. Yoon, C. S. Hwang, and M. Meyyappan, "All-printed triboelectric nanogenerator," *Nano Energy*, vol. 44, pp. 82–88, 2018.

[14] L. Yang, R. Zhang, D. Staiculescu, C. P. Wong, and M. M. Tentzeris, "A novel conformal RFID-enabled module utilizing inkjet-printed antennas and carbon nanotubes for gas-detection applications," *IEEE Antennas Wirel. Propag. Lett.*, vol. 8, pp. 653–656, 2009.

[15] D. I. Moon *et al.*, "A single input mutliple output (SIMO) variation-tolerant nanosensor," *ACS Sensors*, vol. 3, pp. 1782–1788, 2018.

[16] E. Singh, M. Meyyappan, and H. S. Nalwa, "Flexible graphene-based wearable gas and chemical sensors," *ACS Appl. Mater. Interfaces*, vol. 9, pp. 34544–34586, 2017.

[17] M. Cuartero, M. Parilla, and G. A. Crespo, "Wearable potentiometric sensors for medical applications," *Sensors*, vol. 19, 2019, Art. no. 363.

[18] S. Wang *et al.*, "Paper-based chemiluminescence ELISA: Lab-on-paper based on chitosan modified paper device and wax-screen-printing," *Biosens. Bioelectron.* vol. 31, pp. 212–218, 2012.

[19] S. Kumar, C. M. Pandey, A. Hatamie, A. Simchi, M. Willander, and B. D. Malhotra, "Nanomaterial-modified conducting paper: Fabrication, properties, and emerging medical applications," *Global Challenges*, vol. 3, 2019, Art. no. 1900041, doi: 10.1002/gch2.201900041.

[20] D. I. Moon *et al.*, "On-demand printing of wearbale thermotherapy pad," *Adv. Heathcare Mater.*, vol. 9, no. 4, 2020, Art. no. 1901575.

[21] D. I. Lee *et al.*, "All 3D-printed flexible ZnO UV photodetector on an ultraflat substrate," *ACS Sensors*, vol. 5, pp. 1028–1032, 2020.

[22] S. Baek, G. Y. Bae, J. Kwon, K. Cho, and S. Jung, "Flexible pressure-sensitive contact transistors operating in subthreshold regime," *ACS Appl. Mater. Interfaces*, vol. 11, no. 34, pp. 31111–31118, 2019.

[23] B. Kim, Y. Lu, T. Kim, J. W. Han, M. Meyyappan, and J. Li, "Carbon nanotube coated paper sensor for damage diagnosis," *ACS Nano*, vol. 8, pp. 12092–12097, 2014.

[24] S. Amendola, A. Palombi, and G. Marrocco, "Inkjet printing of epidermal RFID antennas by self-sintering conductive ink," *IEEE Trans. Microw. Theory Tech.*, vol. 66, no. 3, pp. 1561–1569, Mar. 2018.

[25] M. A. Ullah, M. T. Islam, T. Alam, and F. B. Ashraf, "Paper-based flexible antenna for wearable telemedicine applications at 2.4 GHz ISM band," *Sensors*, 18, 2018, Art. no. 4214.

[26] R. A. Street *et al.*, "Jet printing flexible displays," *Mater. Today*, vol. 9, pp. 32–37, 2006.

[27] Q. Huang, K. N. Al-Milaji, and H. Zhao, "Inkjet printing of silver nanowires for heaters," *ACS Appl. Nano Mater.*, vol. 1, pp. 4528–4536, 2018.

[28] G. Cummins and M. Desmulliez, "Inkjet printing of conductive materials: A review," *Circuit World*, vol. 38 No. 4, pp. 193–213, 2012.

[29] S. K. Eshkalak, A. Chinnappan, W. A. D. M. Jayathilaka, M. Khatibzadeh, E. Kowsari, and S. Ramakrishna, "A review on inkjet printing of CNT composites for smart applications," *Appl. Mater. Today*, vol. 9, pp. 372–386, 2017.

[30] J. M. Hoey, A. Lutfurakhmanov, D. L. Schulz, and I. S. Akhatov, "A review on aerosol-based direct-write and its applications for microelectronics," *J. Nanotechnol.*, vol. 2012, 2012, Art. no. 324380, doi: 10.1155/2012/324380.

[31] R. P. Gandhiraman, E. Singh, D. C. Diaz-Cartagena, D. Nordlund, J. Koehne, and M. Meyyappan, "Plasma jet printing for flexible substrates," *Appl. Phys. Lett.*, vol. 108, 2016, Art. no. 123103.

[32] A. Dey, S. Krishnamurthy, J. Bowen, D. Nordlund, M. Meyyappan, and R. P. Gandhiraman, "Plasma jet printing and *in situ* reduction of highly acidic graphene oxide," *ACS Nano*, vol. 12, no. 6, pp. 5473–5481, 2018.

[33] A. Dey *et al.*, "Plasma jet based *in situ* reduction of copper oxide in direct write printing," *J. Vac. Sci. Tech. B*, vol. 37, 2019, Art. no. 031203.

[34] E. Gale, "TiO$_2$-based memristors and ReRAM: Materials, mechanisms and models (a review)," *Semicon. Sci. Technol.*, vol. 29, no. 10, 2014, Art. no. 104004.

[35] J. Watson, "The tin oxide gas sensor and its applications," *Sens. Actuators*, vol. 5, no. 1, pp. 29–42, 1984.

[36] B. Kim, Y. Lu, A. Hannon, M. Meyyappan, and J. Li, "Low temperature Pd/SnO$_2$ sensor for carbon monoxide detection," *Sens. Actuators B. Chem.*, vol. 177, pp. 770–775, 2013.

[37] J. W. Han, T. Rim, C. K. Baek, and M. Meyyappan, "Chemical gated field effect transistor by hybrid integration of one-dimensional silicon nanowire and two-dimensional tin oxide thin film for low power gas sensor," *ACS Appl. Mater. Interfaces*, vol. 7, pp. 21263–21269, 2015.

[38] S. Ammu *et al.*, "Flexible, all-organic chemiresistor for detecting chemically aggressive vapors," *J. Am. Chem. Soc.*, vol. 134, no. 10, pp. 4553–4556, 2012.

[39] J. W. Han, B. Kim, J. Li, and M. Meyyappan, "A carbon nanotube based ammonia sensor on cellulose paper," *RSC Adv.*, vol. 4, pp. 549–553, 2014.

[40] B. Kim, T. Newman, R. S. Jones, D. I. Moon, J. W. Han, and M. Meyyappan, "Carboxylated single-walled carbon nanotube sensors with varying pH for the detection of ammonia and carbon dioxide using an artificial neural network," *ACS Appl. Nano Mater.*, vol. 2, pp. 6445–6451, 2019.

[41] Z. Xu *et al.*, "Topic review: Application of raman spectroscopy characterization in micro/nano- machining," *Micromachines*, vol. 9, pp. 1–23, 2018.

[42] A. Hannon, Y. Lu, H. Hong, J. Li, and M. Meyyappan, "Functionalized-carbon nanotube sensor for ammonia detection," *Sensor Lett.*, vol. 12, pp. 1469–1476, 2014.

[43] A. Hannon, Y. Lu, J. Li, and M. Meyyappan, "A sensor array for the detection and discrimination of methane and other environmental pollutant gases," *Sensors*, vol. 16, 2016, Art. no. 1163.